Unexpected cation dynamics in the low-temperature phase of methylammonium lead iodide – the need for improved models

Kacper Drużbicki, Roberto Pinna, Svemir Rudic, Marek Jura, Giuseppe Gorini and Felix Fernandez-Alonso

Published version information

Citation: Druzbicki, K et al. "Unexpected cation dynamics in the low-temperature phase of methylammonium lead iodide – the need for improved models." The Journal of Physical Chemistry Letters, vol. 7 (2016): 4701-4709.

doi: 10.1021/acs.jpclett.6b01822

Unexpected Cation Dynamics in the Low-temperature Phase of Methylammonium Lead Iodide – The Need for Improved Models

Kacper Drużbicki, [†,‡] Roberto Simone Pinna,[§,⊥] Svemir Rudić,[§] Marek Jura,[§] Giuseppe Gorini[‖] and Felix Fernandez-Alonso*[§,⊥]

[†]Faculty of Physics, Adam Mickiewicz University, Umultowska 85, 61-614 Poznan, Poland

[‡]Frank Laboratory of Neutron Physics, Joint Institute for Nuclear Research, 141980, Dubna, Russia

[§]ISIS Facility, Rutherford Appleton Laboratory, Chilton, Didcot, Oxfordshire OX11 0QX, UK

[‖]CNISM, Università degli Studi di Milano-Bicocca, Piazza della Scienza 3, 20126 Milano, Italy

[⊥]Department of Physics and Astronomy, University College London, Gower Street, London, WC1E 6BT, UK

Supporting Information Placeholder

ABSTRACT: High-resolution inelastic neutron scattering and extensive first-principles calculations have been used to explore the low-temperature phase of the hybrid solar-cell material methylammonium lead iodide up to the well-known phase transition to the tetragonal phase at *ca.* 160 K. Contrary to original expectation, we find that the *Pnma* structure for this phase can only provide a qualitative description of the geometry and underlying motions of the organic cation. A substantial lowering of the local symmetry inside the perovskite cage leads to an improved atomistic model that can account for all available spectroscopic and thermodynamic data, both at low temperatures and in the vicinity of the aforementioned phase transition. Further and detailed analysis of the first-principles calculations reveals that large-amplitude distortions of the inorganic framework are driven by both zero-point-energy fluctuations and thermally activated cation motions. These effects are significant down to liquid-helium temperatures. For this important class of technological materials, this work brings to the fore the pressing need to bridge the gap between the long-range order seen by crystallographic methods and the local environment around the organic cation probed by neutron spectroscopy.

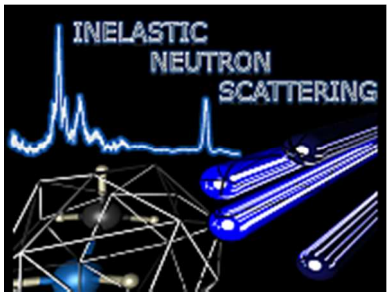

Since its first use as a sensitizer in 2009,[1] methylammonium lead iodide ($CH_3NH_3PbI_3$, hereafter abbreviated MAPI) has emerged as one of the most promising light-absorbing materials for solar-energy applications. When deposited on TiO_2 scaffolds, its light-conversion efficiency exceeds 20%, an unprecedented performance for alternative photovoltaic technologies.[2] Recent advances in MAPI-based solar-cell devices have triggered intense research efforts to establish the fundamental properties of this material. At ambient pressure, three crystallographic phases have been identified as shown in Fig. 1, namely: a high-temperature cubic phase ($Pm\bar{3}m$; T > 327 K); a room-temperature tetragonal phase (*I*4/*mcm*; T > 160 K); and a low-temperature phase (*Pnma*, T < 160 K).[3-4] In the cubic structure, the methylammonium cation (hereafter MA^+) becomes highly disordered along all unit-cell directions, *i.e.,* MAPI becomes a fully fledged plastic crystal.[4] Recent studies have also indicated that the phase transformation to the tetragonal phase results in the tilting of PbI_6 octahedra about the crystallographic *c*-axis, whereby MA^+ adopts four possible orientations characterized by a substantial degree of dynamical disorder.[5]

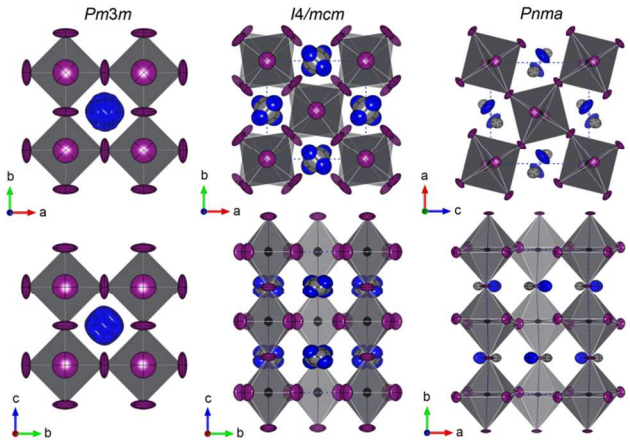

Figure 1. Structures of the three known phases of MAPI at ambient pressure obtained from diffraction studies (lead: black; iodine: purple; nitrogen: blue; carbon: dark grey). For simplicity, hydrogens have been omitted from these images. Left and center: cubic ($Pm\bar{3}m$, T = 350 K) and tetragonal (*I*4/*mcm*, T = 295 K) phases from single-crystal neutron diffraction.[4] Right: *Pnma* structure from single-crystal XRD at T = 100 K.[3] Anisotropic-displacement ellipsoids are given with 90% probability, as obtained from the refinement of crystallographic data (99% for *Pnma*).

Early work solved the low-temperature structure using the $Pna2_1$ space group,[6] yet more recent and comprehensive single-crystal X-Ray Diffraction (XRD) experiments at 100 K by

Baikie *et al.*[3] have revisited this assignment and favor the use of *Pnma* symmetry. Using this space group, centrosymmetric constraints dictate that MA^+ may adopt a single anticlinic orientation relative to the inorganic framework. Baikie *et al.*[3] have also reported unusual features in the Fourier maps, and these have been interpreted qualitatively as abnormal anharmonic displacements of the iodine atoms. Alternatively, it has been surmised that angular distortions of the octahedral may also play a role.[3,7] The interplay between hydrogen-bond (HB) strength and octahedral distortion has been explored further by Lee *et al.*[8] using density-functional-theory (DFT) calculations. It was found that octahedral tilting is stabilized by NH···I interactions with a binding strength proportional to such a distortion. Extension to the tetragonal phase indicates the presence of two distinct types of HB interactions.[9] These findings are also in line with recent molecular dynamics (MD) simulations, which suggest that spontaneous bidirectional ordering of MA^+ underpins the emergence of the tetragonal phase.[10] The potential disturbance of the lead-iodide perovskite lattice by MA^+ motions cannot be ruled out either, and this possibility is consistent with the observation of the aforementioned anomalous diffuse scattering by Baikie *et al.*[3]

From the discussion presented above, one would expect that both the tetragonal and low-temperature phases are related to each other via a continuous distortion of the inorganic perovskite framework. As rightly pointed out by Baikie *et al.* in their seminal XRD work,[3] this view is at odds with the absence of a direct group–subgroup relationship between *I4/mcm* and *Pnma* symmetries – *i.e.,* it is not possible to effect a continuous structural change to transform one phase into the other. It is, therefore, expected that a (possibly transient) intermediate phase may exist, but experimental confirmation of its presence has proven elusive. Instead, it has been recently confirmed that both phases can coexist below the phase transition into the higher-temperature tetragonal structure at *ca.* 160 K.[11] Also, phase coexistence all the way down to 10 K has been observed in thin-film specimens,[12] and recent real-space studies using scanning-tunnelling microscopy at 77 K and 10 K reveal significant deviations from bulk behaviour associated with non-trivial surface-reconstruction and reorientational effects.[13,14] Although it is generally accepted that the *Pnma* phase is devoid of static or dynamical disorder, Fabini *et al.*[15] have recently shown that MAPI can exhibit glassy dynamics at low temperatures, and that these are potentially coupled to local distortions of the PbI_6 sub-lattice.

Taken altogether, these observations pose a number of open questions related to the arrangement and underlying motions of MA^+, as well as on our ability to provide a quantitative description of the low-temperature phase of MAPI consistent will all available experimental data. Spectroscopic techniques sensitive to the local environment can offer additional insights into these, and both tetragonal and low-temperature phases have been the subject of a growing number of such studies, with an emphasis on the use of photon-based spectroscopies.[16-23] These reports have explored quite extensively the far- and mid-infrared (IR) range, spanning optically accessible motions of both MA^+ and its underlying inorganic framework. The interpretation of these spectroscopic data has relied heavily on the use of harmonic lattice-dynamics (HLD) calculations within the framework of solid-state DFT. The upper spectral range above *ca.* 1000 cm^{-1} is dominated by MA^+ modes and their assignment has been reported in earlier works.[16,17,19] The interpretation of spectral features at lower energies remains relatively unexplored. Another complication arises from the lack of separation of MA^+ *vs.* framework modes in the overall optical response, leading to both spectral congestion and a fair degree of ambiguity in the interpretation of these data.

In this work, we use high-resolution Inelastic Neutron Scattering (INS) to probe MA^+ motions and the surrounding environment. Owing to the large incoherent cross section of hydrogen, INS is superbly sensitive to hydrogen motions, as discussed in more detail in Section 1 of the **SI**. Moreover, INS intensities are not subjected to selection rules and, as such, are directly related to the underlying Vibrational Density Of States (VDOS) of the entire (bulk) material, thereby facilitating comparison with theoretical predictions.[24] These features make INS a suitable probe of the local environment and motions of MA^+ in MAPI, enabling a quantitative appraisal of our current understanding of the physico-chemical behavior of this important material.

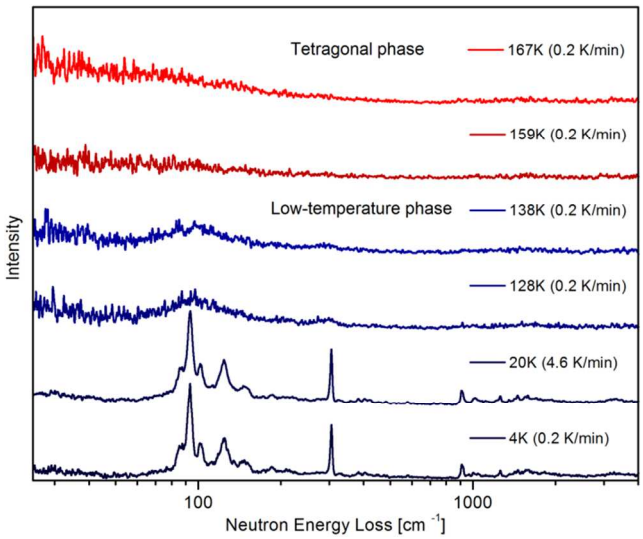

Figure 2. Temperature evolution of the INS spectrum of MAPI obtained at a cooling rate of 0.2 K/min across the phase transition from the tetragonal phase. The legend indicates the average temperature during the cooling runs. The dataset labelled 159 K was collected over the range 165→154 K as the sample crossed the phase transition over a period of *ca.* 1.5 hours and, thus, it contains contributions from both phases. The low-temperature data shown at the bottom of the figure includes the INS spectrum measured at a much-faster cooling rate of 4.6 K/min. For further details, see the main text.

As described in more detail in **EXPERIMENTAL**, INS experiments were carried out on the high-resolution TOSCA spectrometer at the ISIS Pulsed Neutron & Muon Source, Rutherford Appleton Laboratory, UK.[25-27] Figure 2 summarizes our INS results, obtained in the vicinity of the phase transition at T = 162.2 K[6] and at lower temperatures. Qualitatively,

the low-temperature data exhibit a number of sharply defined features in the range 10–400 cm^{-1}. Above this range, spectral intensities fall off very rapidly with increasing energy transfer. This behavior is indicative of strong contributions from so-called phonon wings – *i.e.,* combination bands associated with the simultaneous excitation of internal MA^+ vibrations and lower-energy intermolecular modes.

From inspection of the INS data, it is evident that the spectral response is different above and below 160 K. These changes are also seen as an increase of elastically scattered neutrons as one enters the low-temperature phase. We note that the high-temperature INS data in either phase are quite featureless, and that the low-temperature phase is characterized by the presence of two distinct bands below 400 cm^{-1}. The overall envelope of these features is retained all the way down to 4 K. These results suggest that MA^+ has not been fully frozen and that it remains quite floppy inside the halide cage even after undergoing this phase transition upon cooling. A similar spectral broadening has been reported in recent temperature-dependent Raman studies of MAPI.[28] Figure 2 also shows that the resulting low-temperature INS spectrum is insensitive to the use of slow (0.2 K/min) or fast (4.6 K/min) cooling rates across the phase transition. This is an important result, as it indicates that phase metastability upon entering the low-temperature phase is either very unlikely or very hard to avoid in the first place. Our experimental findings can also be placed in the context of recent quasielastic neutron scattering studies.[29-30] In particular, Chen *et al.,*[26] have interpreted their experimental results in the tetragonal phase in terms of MA^+ motions along four- (C_4) and three-fold (C_3) symmetry axes normal to the C–N bond. According to this work, only C_3 rotations remain active in the low-temperature phase. The persistence of motions at low temperatures is also in line with a relatively small change in hydrogen mean-square displacements reported by Leguy *et al.* [30] when crossing the phase transition at *ca.* 160 K. In a similar vein, Bakulin *et al.*,[31] have used pump-probe ultrafast 2D vibrational spectroscopy to follow the dynamics of MA^+ in the tetragonal phase. This study has revealed two characteristic time constants of motion, identified as fast 'wobbling-in-a-cone' (~300 fs) and slower 'jump-like' reorientations of the molecular dipole with respect to the inorganic lattice (~3 ps). The presence of faster, wobbling-in-a-cone motions is consistent with our INS results as well as the work of Mattoni *et al.*[32] Notwithstanding the insights provided so far by these experimental data, the emergence of an ordered structure via a first-order phase change accompanied by an order-disorder-type transition of the MA^+ ensemble remains a puzzling phenomenon, and recent work has suggested a close interplay between the strength of HBs and octahedral tilting of the inorganic cage, the latter being regarded as a suitable order parameter.[9]

For a quantitative interpretation of the INS data presented above, we have resorted to the use of periodic DFT calculations, and to HLD and Born-Oppenheimer MD (BOMD) methodologies to simulate INS spectra for direct comparison with experiment – for further details, see **COMPUTATIONAL**. Figure 3 shows the most relevant models explored in this work – for more details, see the **SI**. We have made INS predictions using both fully as well as partially optimized models. Full-cell relaxation of the *Pnma* structure was performed with the dispersion-corrected PBE-TS functional. These calculations yielded cell constants a = 9.023 Å, b = 12.691 Å and c = 8.480 Å, in very good agreement with available experimental data (a = 8.816 Å, b = 12.598 Å and c = 8.564 Å).[29]

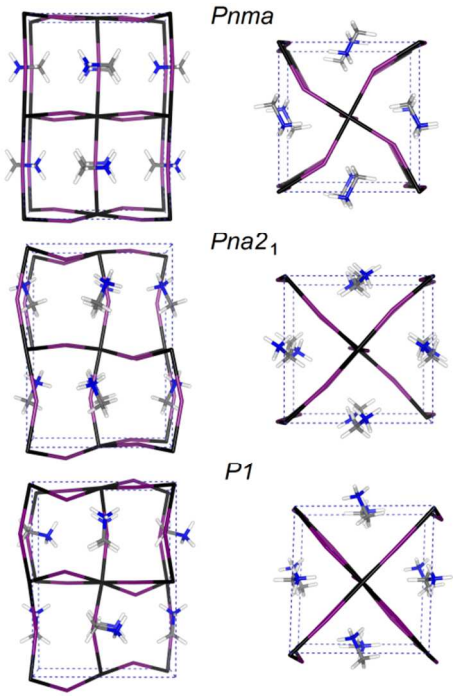

Figure 3. Fully optimized DFT structures for the most relevant low-temperature models explored in this work (*Pnma*, *Pna*2_1 and *P*1). Please note the different MA^+ orientations relative to the inorganic cage in each case. For further details, see the main text and the **SI**.

Figure 4 shows a comparison of the computational predictions against the experimental INS data. Above 1000 cm^{-1}, the spectral response is dominated by internal MA^+ modes. These have been analyzed in detail in previous works[16,17,19,28,32] and, as shown in Fig. 4, can be described satisfactorily using the *Pnma* structure. These internal molecular modes are relatively insensitive to the local environment of the MA^+ cation. In addition to fundamental (0⇒1) band heads in this region, we also observe the presence of multiple higher-order transitions arising from overtones and phonon wings. It is also important to note that *Pnma* provides a fair description of fundamental modes in this range, yet it cannot reproduce at a quantitative level higher-order transitions arising from the coupling to low-energy external modes.

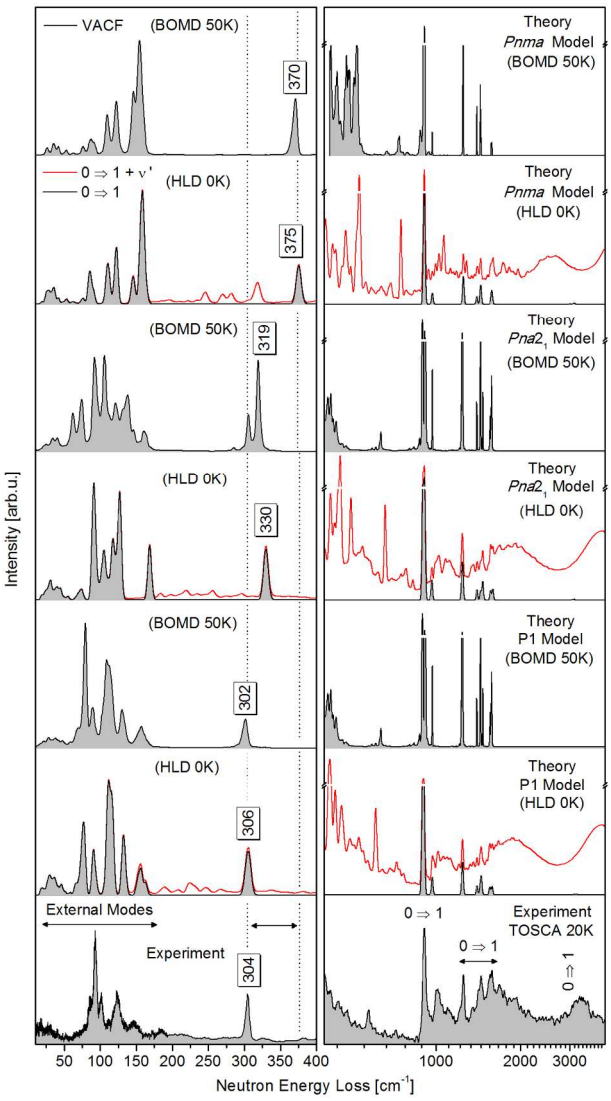

Figure 4. Comparison of experimental and theoretical INS spectra over the range 10-400 cm^{-1} (left) and 400-4000 cm^{-1} (right, note the log-scale for the abscissa). Theoretical spectra have been obtained using both HLD and BOMD calculations. In the latter case, VACF refers to the Velocity Autocorrelation Function, as explained in more detail in **COMPUTATIONAL**. These predictions correspond to the models presented in Fig. 3, calculated via full-cell optimization. For HLD predictions, fundamental transitions ($0 \Rightarrow 1$) are compared to those including overtones and combination bands ($0 \Rightarrow 1 + \nu'$), the latter represented by red lines. We note that the suppression of spectral intensities caused by the Debye-Waller factor is only accounted for by HLD.

In addition to *Pnma*, the other two models shown in Fig. 3 reflect other possible symmetries of the unit cell and these were explored in detail during a systematic search involving several dozens of possible alternatives with and without explicit symmetry constrains – for further details on the search procedure and associated criteria for model selection, see Sections 2 and 3 of the **SI**. Overall, our search revealed a very flat potential energy surface around MA^+, making the calculations increasingly challenging upon a reduction of the number of symmetry operations. One important and quite general finding relates to the coupling of MA^+ to inorganic-cage coordinates. The lead-iodide framework was found to be extremely flexible, its geometry being largely dictated by the specific orientation of MA^+ and the underlying (and dominant) HB interactions with the inorganic cage.

At lower energy transfers, we note the presence of a manifold of closely spaced transitions below 200 cm^{-1}, followed by a single and sharp feature above 300 cm^{-1}. As shown in more detail in Table 1 below and the **SI**, this feature can be assigned in all models to a disrotatory mode and it is particularly sensitive to the local MA^+ environment. The results shown in the left panels of Fig. 4 also serve to demonstrate that the specific orientation of MA^+ has a marked impact on the resulting INS response below 400 cm^{-1}. For *Pnma*, MA^+ is preferentially oriented along the perpendicular to the long axis of the unit-cell on the *ac* plane, as shown in Fig. 3. For this model, we find that HLD calculations greatly overestimate the frequency of the feature observed experimentally at 304 cm^{-1}. BOMD results can help us capture non-harmonic corrections to this transition energy and show a very slight shift of this mode, from 375 down to 370 cm^{-1}. Also, we note that all solid-state calculations for the low-temperature phase reported in the literature predict the appearance of this feature at 350 – 400 cm^{-1}, as recently presented in Refs. 17 and 32. Moreover, both HLD and BOMD calculations using *Pnma* predict a prominent and inverted band head peaking at *ca.* 150 cm^{1}, in contrast with the reverse trend seen in the experimental INS data. Similar considerations apply to $Pna2_1$, where the C-N axis is preferentially oriented parallel to the long axis of the unit cell. In this case the isolated mode above 300 cm^{-1} is still overestimated and the relative intensities and positions of lower-lying modes below 200 cm^{-1} do not match those seen in the INS data, even if experimental cell volumes are used in the calculation. Similarly, other high-symmetry alternatives including $P2_1$, $P2_1/c$, Pc and $P2_12_12_1$ do not describe of the experimental INS data in a quantitative fashion.

From the analysis presented above, we can conclude that *Pnma* and $Pna2_1$ can only provide a qualitative description of the INS data. At a more quantitative level, the lower-symmetry $P1$ model provides the best quantitative match to the experimental INS data, as shown by the corresponding BOMD spectrum. In particular, this model can account for the additional (and weak) features observed in the range 300-400 cm^{-1} by including overtone and combination bands arising from the stronger features at lower energy transfers. From these INS data, we find no evidence to indicate the presence of other dominant geometries at low temperatures. The performance of a wide range of DFT exchange-correlation functionals to describe the INS data is reported in Section 2 of the **SI**. As figures of merit, this analysis has considered the overall agreement between experiment and calculation, as well as the location of the aforementioned spectral feature at 300 cm^{-1}. From this exercise, we conclude that our level of confidence that the $P1$ model constitutes an improved description of the INS results using state-of-the-art DFT is >95%. In terms of local structure, the organic cation in this model is oriented in

both vertical and horizontal directions with equal probability. As such, this model is reminiscent of the higher-temperature tetragonal phase. A more detailed description is given in Section 3 of the **SI**, where it is also shown that the INS data is insensitive to the periodicity of the *P1* unit cell used in the PW-DFT calculations. To facilitate comparison with *Pnma* and $Pna2_1$, the *P*1 model is based on a *Z*=4 symmetry-unconstrained superstructure, although it can be further simplified to a *Z*=2 primitive cell corresponding to *Cc* symmetry. This primitive cell is shown in Fig. 5, in order to illustrate its main structural motifs in the immediate vicinity of MA^+. These alternative views of the *P*1 model result in indistinguishable INS spectra and, therefore, are equivalent representations of the same local structure around MA^+ in MAPI. As such, our *P*1 model constitutes a suitable starting point for more detailed structure-search studies using experimental probes that are sensitive to both intermediate- and long-range order.[33,34] Sections 1 and 3 of the **SI** provide a more detailed discussion of the additional assumptions required to bridge the long-range order seen by XRD and the local environment around MA^+ as probed in this work via INS. One should further note that a *Cc* space group is acentric and, therefore, our model is consistent with previous findings by Filippetti *et al.*[35] in which the low-temperature phase of MAPI may be viewed as a disordered super-paraelectric exhibiting spontaneous polarization at the nanoscale and polar compensation at the macroscale.

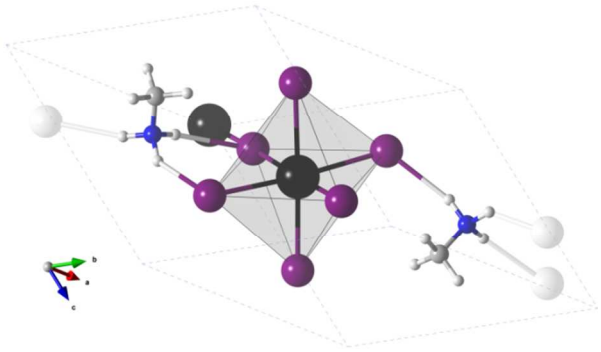

Figure 5. Primitive cell with *Z*=2 and *P*1 symmetry. Iodine atoms outside the cell boundaries are represented as translucent balls.

The top panel in Fig. 6 shows the experimental INS spectrum below 400 cm^{-1} along with optical-spectroscopic data reported in the literature.[22-23] To facilitate comparison, spectral features in the INS data are labeled *a* thru *o*, starting from the highest-energy feature at 304 cm^{-1}. The first thing to note is that both INS and optical data share a number of common features below 200 cm^{-1}, although the intense triplet around 90 cm^{-1} is only present in the INS data. Figure 6 also presents BOMD and HLD predictions of the INS data using the *P*1 model. In particular, the BOMD INS spectrum provides a superb description of the INS data. We can further decompose the BOMD VDOS in terms of CH_3 and NH_3^+ contributions where, as expected on purely qualitative grounds, the INS response is dominated by hydrogen motions. This analysis also shows that the isolated spectral feature at 304 cm^{-1} is primarily associated with NH_3^+ motions, whereas at lower energies both CH_3 and NH_3^+ groups contribute in a similar way to the observed spectral intensities. These BOMD calculations can reproduce at a quantitative level all observed spectroscopic transitions.

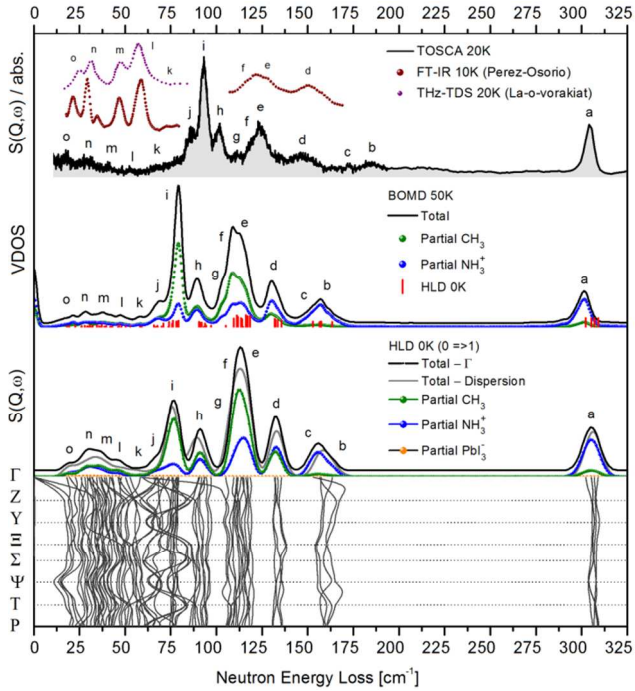

Figure 6. Spectroscopic data (top abcissa) and detailed analysis using the *P*1 model (bottom abscissa). Top: available experimental data at low energies including the INS spectrum (this work), as well as FT-IR and THz-TDS data from Refs. 22 and 23, respectively. For clarity, different optical datasets have been offset along the ordinate axis by arbitrary constants. Middle: partial and total VDOSs from BOMD calculations. Bottom: partial and total VDOSs using HLD with and without dispersion. To facilitate comparison with experimental data, all VDOSs have been weighted by their corresponding neutron cross sections. A more detailed comparison over the entire spectral range as well as normal-mode animations are given in the **SI**.

The HLD predictions shown in Fig. 6 have been further dissected into CH_3, NH_3^+, and PbI_3^- contributions, further confirming the BOMD results presented above. We also compare calculations at the Γ-point to those including full mode dispersion, and observe very similar results in both cases for those bands associated with MA^+ vibrations. These similarities imply that MA^+ motions are primarily local in nature, with little long-range coupling across cages. PbI_3^- modes contribute up to around 120 cm^{-1} and these modes exhibit a more pronounced dispersive character. Further, comparison of HLD with BOMD results also shows that anharmonicity has a more marked effect on relative intensities than on band positions, particularly for MA^+ modes labeled *e-j* in the figure. Within the HLD framework, we can further decompose the INS response in terms of normal modes and a detailed assignment of

these is shown in Table 1 and the **SI**. The most intense feature at 93 cm^{-1} (labelled *i*) corresponds to $\circlearrowleft$(N-CH_3) librations. This mode can only be observed via INS, as the Raman activity of this band is related to ν(Pb-I) contributions rather than to MA^+ motions. The most significant deviations in our predictions correspond to bands *b* and *c*, observed at 182 and 173 cm^{-1} and underestimated by the calculations by 15-20 cm^{-1} (see also Fig. 6). These bands arise from NH_3^+ librations and hydrogen-bridge ν(N-H···I) stretches. The corresponding average NH···I distances obtained from 50-ps BOMD trajectories at 50 K are 2.589, 2.594, and 2.633 Å for *Pnma*, *Pna*2_1, and *P*1 models, respectively. Although these distances compare well with an experimental value of 2.613 Å,[5] the INS results suggest that the PBE-TS exchange-correlation functional tends to underestimate the strength of these interactions.

Table 1 Comparison to experiment and spectroscopic assignments using the *P*1 model. Superscripts *a-o* correspond to those shown in Fig. 6. Hyperlinks to computer animations of all normal modes can be found in Table S1 of the **SI**.

ν [cm^{-1}]			Assignment
INS	HLD	BOMD	
3141	3093	3108	ν(CH) + ν(NH)
1584	1588	1585	$\delta(NH_3^+)$
1557	1558	1560	
1448	1456	1454	
1413	1402	1402	$\delta_{sym}(CH_3)$
1253	1249	1240	$\rho(NH_3^+)$ + $\rho(CH_3)$
911	898	896	
304[a]	306	302	*disrotatory* $\tau(NH_3^+)$-$\tau(CH_3)$
182[b]	157	157	*lib.* $\circlearrowleft$ (C-NH_3^+) / ν(NH···I)
173[c]	153	153	
146[d]	132	130	*lib.* $\circlearrowleft$ (C-NH_3^+) / ν(NH···I) + $\tau(CH_3)$
124[e]	116	115	*lib.* $\circlearrowleft$ ($CH_3NH_3^+$)
118[f]	111	109	*lib.* $\circlearrowleft$ (N-CH_3) / $\tau(CH_3)$ + $\nu(PbI_6)$ $E_g(O_h)$
110[g]	105	106	*lib.* $\circlearrowleft$ (N-CH_3) + ν(Pb-I)
102[h]	91	90	
93[i]	79	79	
87[j]	71	68	
66[k]	58	58	δ(I-Pb-I) $T_{1u}(O_h)$
53[l]	47	47	rocking / twisting PbI_6 deformation
40[m]	37	38	
30[n]	31	28	
18[o]	23	21	$\circlearrowleft$ (PbI_6) / *transl.* ⇒ Pb

Our predictions also allow for a robust assignment of previous FT-IR,[22] Raman,[16] and MD[32] results reported in the literature. Specifically, the distinct and isolated feature observed at 304 cm^{-1} and associated with disrotatory $\tau(NH_3^+)$-$\tau(CH_3)$ motions retains its character across all models investigated in this work, as it corresponds to a normal mode of vibration that is largely decoupled from framework vibrations and is not mixed with other internal modes. As such, its degenerate character in the INS data imposes strong constraints on the adequacy of the underlying structural model to describe the INS data. Furthermore, this feature is not Raman-active and, therefore, cannot be assigned to the broad Raman feature observed by Quarti *et al.*[16] at *ca.* 250 cm^{-1}. This feature has also been reported in MD simulations of a tightly bound cation using *Pnma*.[32] The recent assignment of this elusive transition by Ledinský *et al.*[20] as a resonantly enhanced second-order Raman signal thus appears to be more a more reasonable assignment, given the absence of fundamentals in the range 190-300 cm^{-1}. Features *a,d,* and *f* in Fig. 6 have been previously reported by Pérez-Osorio *et al.*[23] using FT-IR and are assigned in Table I. Using the HLD calculations, we can also make specific predictions of thermodynamic properties as a function of temperature. These results are shown in Section 4 of the SI. In particular, Fig. S11 shows the temperature dependence of the molar heat capacity compared with the recent experimental results of Fabini *et al.*[15] Below 100 K, the agreement between experiment and our computational predictions for *Pna*2_1 and the *P*1 is excellent, whereas *Pnma* tends to underestimate this observable in a systematic fashion. Along with the higher total free energy relative to *Pna*2_1 and *P*1 shown in Fig. S10, this result confirms the inadequacy of the *Pnma* model to describe MAPI at a quantitative level. Also, these heat-capacity data show that a phonon-based description of atomic motions starts breaking down at *ca.* 100 K, a result which is entirely in line with the experimental INS data presented in Fig. 2, as well as with an increasing contribution of stochastic motions associated with MA^+ reorientations within the perovskite cage.

As an additional and independent check of our predictions, we have performed BOMD calculations in the vicinity of the phase transition to the tetragonal phase. A comparison of these calculations with experiment is shown in Fig. 7. Once more, we note that the *P*1 model provides a quantitative description of the experimental data relative to the qualitative agreement of either *Pnma* or *Pna*2_1. In particular, the broad band originating from orientationally averaged disrotatory $\tau(NH_3^+)$-$\tau(CH_3)$ motions moves below 300 cm^{-1} at these temperatures and is reproduced quantitatively by the *P*1 model, whereas *Pnma* or *Pna*2_1 predict the position of this feature *ca.* 100 cm^{-1} above. This finding indicates that the potential-energy landscape around MA^+ is considerably softer than previously anticipated and also explains why our experimental INS data differ from the MA^+-projected VDOSs recently reported by Mattoni *et al.*[32] using *Pnma*. More recent BOMD results by Lahnsteiner *et al.*[36] also highlight qualitative and non-trivial differences between the reorientational dynamics of the low-, intermediate-, and high-temperature phases of MAPI, whereby dynamical correlations between neighbouring MA^+ cations show a maximum at room temperature, whereas in the lower- and higher-temperature phases these motions are less correlated. Figure S13 in the **SI** shows a more detailed evolution of BOMD spectra as a function of temperature, where the onset of significant spectral broadenings starts at *ca.* 60 K, in agreement with the slowing-down in relaxation dynamics upon cooling observed by Fabini *et al.*[15] This onset also sheds light on recent findings on the thermal conductance of MAPI films in the low-temperature phase,[37] where a Debye-Gallaway model becomes invalid just above 60 K and the temperature-dependence of the thermal conductivity can only be described with a glass-like model. We also note that Filippetti *et al.*[35] have reported that clear ferroelectric behaviour can only be observed below 40−50 K when considering planar disorder of *Pm* symmetry. At higher temperatures, the polarization is

expected to be progressively suppressed as ferroelectric ordering is hindered by a large configurational entropy, findings which are consistent with our experimental and computational results.

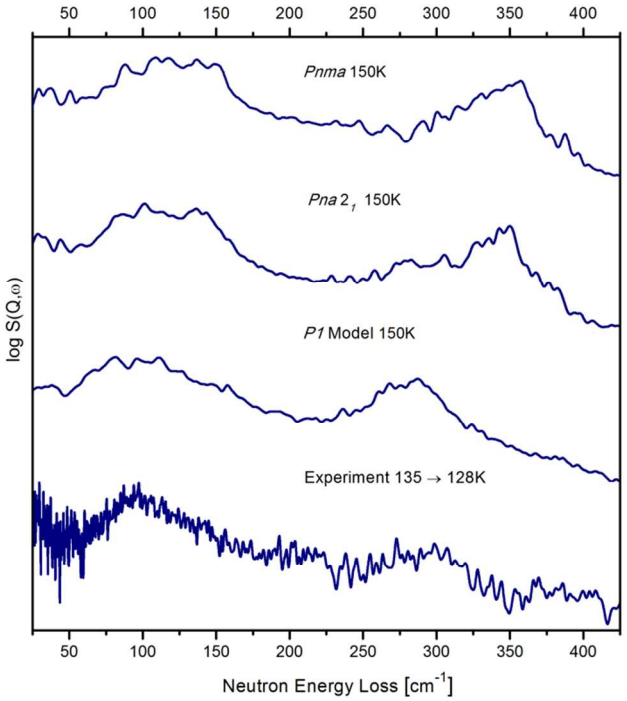

Figure 7. Low-energy INS spectra of the low-temperature phase of MAPI in the vicinity of the phase transition to the tetragonal phase. Bottom: experimental data. Other traces correspond to BOMD predictions using the PBE-TS functional. For further details, see the main text and the **SI**.

We also recall that the *Pnma* crystallographic structure of MAPI has been obtained from single-crystal XRD at 100 K.[3] At this temperature, our BOMD results show that the reorientational dynamics of MA^+ is very pronounced, and that these motions are strongly coupled to the surrounding cage. This behavior is quite evident in the temperature dependence of BOMD spectra shown in Fig. S13 in the **SI**, where the intensity of the two bands at 95 and 125 cm^{-1} (features *i* and *e* in Table 1) grow quite considerably. These two bands originate from HB-hindered MA^+ librations and their overall amplitude reflects distortions of the halide cage. These findings provide a starting point to account for the unusual behavior seen by Baikie *et al.*[3] in their Fourier maps and interpreted as anharmonic displacements of the iodine atoms. Figures S14-S17 in the **SI** confirm this picture. These images show cumulative BOMD coordinates at 100 and 150 K for the three models presented in detail in this work, as well as how these compare with the average atomic positions obtained from the aforementioned XRD studies. The first thing to note is the massive spatial delocalization of MA^+ at these temperatures, a situation where average atomic positions certainly cannot be taken as robust structural descriptors. Moreover, the PbI_3^- cage is far from being a static spectator of MA^+ motions. This is particularly the case for the iodine atoms, which respond quite sensitively to the proximity and relative orientation of MA^+ via H···I bonding. These motions have characteristic energies around 90 cm^{-1} (see features *h-j* in Table 1). This situation persists down to temperatures below 20 K, where the spatial delocalization of hydrogen is still considerable due to zero-point-energy fluctuations involving a large number of normal modes with mixed MA^+-PbI_3^- character (*cf.* Table 1 above and Table S3 in the **SI**). In particular, the most significant angular distortions of PbI_6 octahedra occur at energies below 50 cm^{-1} and the lowest-lying optical transitions predicted at *ca.* 20 cm^{-1} still involve considerable MA^+ motions with mixed rotational-translational character.

In view of the growing interest in understanding phase coexistence and metastability and their relation to the photophysical properties of MAPI,[11,12,38] Table S2 in the **SI** provides a summary of calculated properties of *Pnma, Pna*2_1, and *P1*, bearing in mind that these predictions assume perfect long-range periodicity based on these unit-cell structures and, therefore, exclude yet-to-be-explored possibilities such as cell doubling, or the presence of domains or grain boundaries in the real material – *cf.* Sections 1 and 3 in the **SI**. These properties include cell parameters, total electronic energies, and associated band gaps. Although the shapes of both unit cells are very similar, the *P1* model is characterized by a slightly larger unit-cell volume, a higher electronic energy, and a lower electronic band gap,. As explained in more detail in Section 3 in the SI, the reported unit-cell structure associated with the *P1* model is best viewed as a building block of intermediate and long-range order in the real material. We also emphasize that bridging the local environment around MA^+ (as probed by INS in this work) and the long-range order of the perovskite cage seen by crystallographic techniques remains an open challenge to the field.

In conclusion, the combined use of high-resolution INS experiments and state-of-the-art first-principles calculations has provided, for the first time, a detailed and quantitative view of the local environment and dynamics of MA^+ and its surrounding inorganic framework in the low-temperature phase of MAPI. We find that this phase is characterised by a highly disordered and mobile MA^+ both at low temperatures and in the vicinity of the transition to the tetragonal phase at 160 K. A substantial lowering of the local symmetry relative to *Pnma* is needed to attain quantitative agreement with available spectroscopic (INS and optical) as well as thermodynamic data. The present work, therefore, provides further impetus to understand at a fundamental level the structural and dynamical behaviour of the low-temperature phase of MAPI, as well as suggests that the metastable character of this phase cannot be ruled out at present, rendering this material far more interesting than previously anticipated. As such, the improved model introduced in this work constitutes a suitable starting point for more detailed structure-search studies to describe intermediate- and long-range order in MAPI. At this point in time, we anticipate that this goal could be achieved via a detailed analysis of both Bragg features and underlying diffuse scattering of

neutron and X-ray diffraction data as a function of temperature using pair-distribution-function analysis in conjunction with additional spectroscopic input and computational modelling. From a physico-chemical viewpoint, our analysis also reveals that motions associated with MA^+ and the inorganic framework are inextricably coupled to each other all the way down to liquid-helium temperatures. We also emphasize that the HLD calculations performed in this work include (to first-order) zero-point-energy effects associated with the quantum nature of atomic motions. These appear to affect quite significantly both the structure and dynamics of the MA^+ moiety in MAPI, and also call for the full inclusion of nuclear motions in the description of its optical response and photovoltaic performance by taking advantage of recent and exciting methodological developments.[39]

EXPERIMENTAL

Sample preparation A 5-gram powder sample of MAPI (CAS No 69507-98-8, purity >99%) was purchased from *Xi'an Polymer Light Technologies* and used as received. Prior to the INS experiments, the integrity and crystallinity of the specimen was checked at room temperature using a Rigaku Mini-Flex 600 X-ray diffractometer.[40]

Inelastic neutron scattering High-resolution INS measurements using a total sample mass of 4.3 g contained in a vacuum-tight flat aluminium cell of cross-sectional area 4x4 cm^2 were performed on the TOSCA spectrometer at the ISIS Pulsed Neutron & Muon Source, Rutherford Appleton Laboratory, United Kingdom.[25-27] TOSCA is a so-called inverted-geometry neutron spectrometer spanning energy-transfers up to 4000 cm^{-1}. The spectral resolution of TOSCA is comparable to more conventional infrared and Raman techniques, and amounts to *ca.* 2% across the spectral range of interest to this work. Numerous examples of TOSCA data can be found in Ref. 41. In this particular study, sample temperatures ranged from 4 to 180 K during data acquisition. Sample cooling was achieved via the use of a dedicated closed-cycle helium refrigerator. Additional heaters and sensors directly attached to the sample enabled fine temperature control over this temperature range.

COMPUTATIONAL

First-principles calculations The periodic Plane-Wave (PW) DFT calculations presented in the main text were performed with the CASTEP 16.1 code.[42] The initial unit cell was constructed based on the *Pnma* structure reported in Ref. 3 using the cell constants measured by Chen *et al*. at T = 4 K.[29] Alternative models were examined by modifying this reference structure and a detailed account of this procedure can be found in Section 3 of the SI. The computations were performed using fixed and fully relaxed cell methodologies at atmospheric pressure. Exchange and correlation were defined all throughout with the Perdew–Burke–Ernzerhof (PBE) functional[43] with the addition Tkatchenko-Scheffler (TS) dispersion corrections,[44] hereafter referred to as PBE-TS. Core electrons were represented via the use of norm-conserving pseudopotentials, and electronic wave functions were expanded using a PW basis set with a kinetic-energy cutoff of 900 eV. The *k*-point grid was adjusted to maintain a constant spacing in reciprocal space of 0.05 $Å^{-1}$, and the self-consistent-field energy was converged with a tolerance of 1×10^{-12} eV per atom. For geometry optimization, Hellmann–Feynman forces acting on individual ions were minimised down to 10^{-5} eV and the associated stress components converged to within 10^{-4} GPa. These choices of the level of theory and convergence criteria have been shown to be adequate for a quantitative description of the spectral response of HB systems at low energy transfers, as recently illustrated in Refs. 45-46. HLD calculations at zero temperature were performed using Density-Functional Perturbation Theory (DFPT) as currently implemented in the CASTEP code.[47] These calculations provide phonon frequencies and associated eigenvectors as input for the simulation of neutron observables. HLD-derived INS spectra were modeled within the incoherent approximation using the aClimax program.[48-49] HLD is a suitable framework to describe the low-temperature INS data and allows for the inclusion of the Debye-Waller factor in these calculations, which reproduce the strong suppression of INS features above 1000 cm^{-1} in MAPI. In order to study anharmonic corrections and thermally induced spectral broadenings at higher temperatures, BOMD simulations were also performed for selected models without symmetry constraints. We recall that these simulations assume that nuclear motions can be treated classically and, therefore, their realm of applicability is restricted to the higher temperatures. Calculated Debye temperatures using HLD and shown in Fig. S12 of the **SI** show that BOMD becomes an adequate approach above 25-30 K. These BOMD simulations were performed using the same numerical settings and the same *k*-point spacing. In this case, self-consistent-field convergence criteria were reduced to 2.5×10^{-8} eV per atom. BOMD calculations were performed up to temperature range 150 K using the canonical (NVT) ensemble with a Nose–Hoover thermostat. Cell volumes were kept fixed to those obtained at zero temperature using PBE-TS. A time step of 0.5 fs was used all throughout. NVT ensemble temperatures were equilibrated for 5 ps, followed by NVE production runs of at least 50 ps. From these production runs, VDOS were obtained via the Fourier-cosine integral transform of the VACF using the nMoldyn code.[50]

ACKNOWLEDGMENT

The authors thank the anonymous referees for a detailed set of insightful comments on the original submission of this work. The UK Science & Technology Facilities Council is acknowledged for financial support, and access to beam time and laboratory equipment at the ISIS Facility. This research was partially supported by the PLGrid Infrastructure, the PROMETHEUS facility (Grant IDs latticedynamics, lattice-

dynamics02), and the 2014-2020 CNR-STFC Agreement for collaborative scientific research at ISIS.

AUTHOR INFORMATION

Corresponding Author

*E-mail: felix.fernandez-alonso@stfc.ac.uk

ASSOCIATED CONTENT

Supporting Information

Comparison of diffraction and INS observables, influence of exchange-correlation DFT functionals on INS spectra, current and alternative models, thermodynamic properties, ab-initio molecular dynamics, detailed spectroscopic assignments, and normal-mode animations.

REFERENCES

(1) Kojima, A.; Teshima, K.; Shirai, Y.; Miyasaka, T. Organometal Halide Perovskites as Visible-Light Sensitizers for Photovoltaic Cells *J. Am. Chem. Soc.*, **2009**, *131*, 6050−6051.

(2) Adams, A.M.; Marin-Beloqui, J.M.; Stoica, G.; Palomares, E. The Influence of the Mesoporous TiO_2 Scaffold on the Performance of Methyl Ammonium Lead Iodide (MAPI) Perovskite Solar Cells: Charge Injection, Charge Recombination and Solar Cell Efficiency Relationship. *J. Mater. Chem. A*, **2015**, *3*, 22154−22161.

(3) Baikie, T.; Fang, Y.; Kadro, J.M.; Schreyer, M.; Wei, F.; Mhaisalkar, S.G.; Graetzel, M; White, T.J. Synthesis and Crystal Chemistry of the Hybrid Perovskite $(CH_3NH_3)PbI_3$ for Solid-State Sensitised Ssolar Cell Applications. *J. Mater. Chem. A*, **2013**, *1*, 5628−5641.

(4) Ren, Y.; Oswald, I.W.H.; Wang, X.; McCandless, G.T.; Chan, J.Y. Orientation of Organic Cations in Hybrid Inorganic–Organic Perovskite $CH_3NH_3PbI_3$ from Subatomic Resolution Single Crystal Neutron Diffraction Structural Studies. *Cryst. Growth Des.,* **2016**, *16*, 2945−2951.

(5) Weller, M.T.; Weber, O.J.; Henry, P.F.; Di Pumpo, A.M.; Hansen, T.C. Complete Structure and Cation Orientation in the Perovskite Photovoltaic Methylammonium Lead Iodide Between 100 and 352 K. *Chem. Commun.,* **2015**, *51*, 4180−4183.

(6) Poglitsch, A.; Weber, D. Dynamic Disorder in Methylammoniumtrihalogenoplumbates (II) Observed by Millimeter-Wave Spectroscopy. *J. Chem. Phys.*, **1987**, *87*, 6373−6378.

(7) Worhatch, R.J.; Kim, H-J.; Swainson, I.P.; Yonkeu, A.L.; Billinge, S.J.L. Study of Local Structure in Selected Organic–Inorganic Perovskites in the $Pm\bar{3}m$ Phase. *Chem. Mater.*, **2008**, *20*, 1272−1277.

(8) Lee, J-H.; Bristowe, N.C.; Bristowe, P.D.; Cheetham, A.K. Role of Hydrogen-Bonding and its Interplay With Octahedral Tilting in $CH_3NH_3PbI_3$. *Chem. Commun.*, **2015**, *51*, 6434−6437.

(9) Lee, J.H.; Lee, J-H.; Kong, E-H.; Jang; H.M. The Nature of Hydrogen-Bonding Interaction in the Prototypic Hybrid Halide Perovskite, Tetragonal $CH_3NH_3PbI_3$. *Sci Rep.*, **2016**, *6*, 21687:12.

(10) Deretzis, I.; Di Mauro, B.N.; Alberti, A.; Pellegrino, G.; Smecca, E.; La Magna, A. Spontaneous Bidirectional Ordering of $CH_3NH_3^+$ in Lead Iodide Perovskites at Room Temperature: The Origins of the Tetragonal Phase. *Sci Rep.*, **2016**, *6*, 24443:7.

(11) Kong, W.; Ye, Z.; Qi, Z.; Zhang, B.; Wang, M.; Rahimi-Iman, A.; Wu, H. Characterization of an Abnormal Photoluminescence Behavior upon Crystal-Phase Transition of Perovskite $CH_3NH_3PbI_3$ *Phys. Chem. Chem. Phys.*, **2015**, *17*, 16405−16411.

(12) Tahara, H.; Endo, M.; Wakamiya, A.; Kanemitsu, Y. Experimental Evidence of Localized Shallow States in Orthorhombic Phase of $CH_3NH_3PbI_3$ Perovskite Thin Films Revealed by Photocurrent Beat Spectroscopy *J. Phys. Chem. C*, **2016**, *120*, 5347−5352.

(13) Ohmann, R.; Ono, L.K.; Kim, H.-S.; Lin, H.; Lee, M.V.; Li, Y.; Park, N.-G.; Qi, Y. Real-Space Imaging of the Atomic Structure of Organic–Inorganic Perovskite. *J. Am. Chem. Soc.,* **2015**, *137,* 16019−16054.

(14) She, L.; Liu, M.; Zhong, D. Atomic Structures of $CH_3NH_3PbI_3$ (001) Surfaces. *ACS Nano*, **2016**, *10,* 1126−1131.

(15) Fabini, D.H.; Hogan, T.; Evans, H.A.; Stoumpos, C.C.; Kanatzidis, M.G.; Seshadri, R. Dielectric and Thermodynamic Signatures of Low-Temperature Glassy Dynamics in the Hybrid Perovskites $CH_3NH_3PbI_3$ and $HC(NH_2)_2PbI_3$. *J. Phys. Chem. Lett.,* **2016**, *7*, 376−381.

(16) Quarti, C.; Grancini, G.; Mosconi, E.O; Bruno, P.; Ball, J.M.; Lee, M.M.; Snaith, H.J.; Petrozza, A.; De Angelis**,** F. The Raman Spectrum of the $CH_3NH_3PbI_3$ Hybrid Perovskite: Interplay of Theory and Experiment. *J. Phys. Chem. Lett.*, **2014**, *5*, 279−284.

(17) Brivio, F.; Frost, J.M.; Skelton, J.M.; Jackson, A.J.; Weber, O.J.; Weller, M.T.; Goni, A.R.; Leguy, A.M.A.; Barnes, P.R.F.; Walsh, A. Lattice Dynamics and Vibrational Spectra of the Orthorhombic, Tetragonal, and Cubic Phases of Methylammonium Lead Iodide. *Phys. Rev. B.*, **2015**, *92*, 144308:8.

(18) Mattoni, A.; Filippetti, A.; Saba, M.I.; Delugas, P. Methylammonium Rotational Dynamics in Lead Halide Perovskite by Classical Molecular Dynamics: The Role of Temperature. *J. Phys. Chem. C*, **2015**, *119*, 25703−25718.

(19) Niemann, R.G.; Kontos, A.G.; Palles, D.; Kamitsos, E.I.; Kaltzoglou, A.; Brivio, F.; Falaras, P.; Cameron, P.J. Halogen Effects on Ordering and Bonding of $CH_3NH_3^+$ in $CH_3NH_3PbX_3$ (X = Cl, Br, I) Hybrid Perovskites: A Vibrational Spectroscopic Study. *J. Phys. Chem. C*, **2016**, *120*, 2509−2519.

(20) Ledinský, M.; Löper, P.; Niesen, B.; Holovský, J.; Moon, S-J.; Yum, J-H.; De Wolf, S.; Fejfar, A.; Ballif, C. Raman Spectroscopy of Organic–Inorganic Halide Perovskites. *J. Phys. Chem. Lett.*, **2015**, *6*, 401−406.

(21) Glaser, T.; Müller, C.; Sendner, M.; Krekeler, C.; Semonin, O.E.; Hull, T.D.; Yaffe, O.; Owen, J.S.; Kowalsky, W.; Pucci, A. *et al.* Infrared Spectroscopic Study of Vibrational Modes in Methylammonium Lead Halide Perovskites. *J. Phys. Chem. Lett.*, **2015**, *6*, 2913−2918.

(22) La-o-Vorakiat, C.; Xia, H.; Kadro, J.; Salim, T.; Zhao, D.; Ahmed, T.; Lam, Y.M.; Zhu, J-X.; Marcus, R.A.; Michel-Beyerle, M-E. *et al.* Phonon Mode Transformation Across the Orthohombic–Tetragonal Phase Transition in a Lead Iodide Perovskite $CH_3NH_3PbI_3$: A Terahertz Time-Domain Spectroscopy Approach. *J. Phys. Chem. Lett.*, **2016**, *7*, 1−6.

(23) Pérez-Osorio, M.A.; Milot, R.L.; Filip, M.R.; Patel, J.B.; Herz, L.M.; Johnston, M.B.; Giustino, F. Vibrational Properties of the Organic–Inorganic Halide Perovskite $CH_3NH_3PbI_3$

from Theory and Experiment: Factor Group Analysis, First-Principles Calculations, and Low-Temperature Infrared Spectra. *J. Phys. Chem. C*, **2015**, *119*, 25703−25718.
(24) Price, D.L.; Fernandez-Alonso, F. in *Neutron Scattering – Fundamentals,* ed. Fernandez-Alonso, F.; Price, D.L. Academic Press, 2013, pp. 1-136.
(25) www.isis.stfc.ac.uk/instruments/tosca (26 Oct 2016).
(26) Pinna, R.S.; Rudić, S.; Parker, S.F.; Gorini, G.; Fernandez-Alonso, F. Monte Carlo Simulations of the TOSCA Spectrometer: Assessment of Current Performance and Future Upgrades. *EPJ Web of Conferences,* **2015**, *83,* 03013−5.
(27) Parker, S.F.; Fernandez-Alonso, F.; Ramirez-Cuesta, A.J.; Tomkinson, J.; Rudić, S.; Pinna, R.S.; Gorini, G.; Fernández Castañón, J. Recent and Future Developments on TOSCA at ISIS. *J. Phys.: Conf. Ser.,* **2014**, *554*, 012003−9.
(28) Leguy, A.M.A.; Goñi, A. R.; Frost, J.M.; Skelton, J.; Brivio, F.; Rodríguez-Martínez, X.; Weber, O.J.; Pallipurath, A.; Alonso, M.I.; Campoy-Quiles, M.; et al. Dynamic Disorder, Phonon Lifetimes, and the Assignment of Modes to the Vibrational spectra of Methylammonium Lead Halide Perovskites. *Phys. Chem. Chem. Phys.,* **2016,** advanced article online dx.doi.org/10.1039/C6CP03474H (26 Oct 2016).
(29) Chen, T.; Foley, B.J.; Ipek, B.; Tyagi, M.; Copley, J.R.D.; Brown, C.M.; Choi, J.J.; Lee, S-H. Rotational Dynamics of Organic Cations in the $CH_3NH_3PbI_3$ Perovskite. *Phys. Chem. Chem. Phys.*, **2015**, *17*, 31278−31286.
(30) Leguy, A.M.A.; Frost, J.M.; McMahon, A.P.; Sakai, V.G.; Kockelmann, W.; Law, C.; Li, X.; Foglia, F.; Walsh, A.; O'Regan, *et al.*. The Dynamics of Methylammonium Ions in Hybrid Organic–Inorganic Perovskite Solar Cells. *Nat. Commun.,* **2015**, *6*, 7124:11.
(30) Leguy, A.M.A.; Frost, J.M.; McMahon, A.P.; Sakai, V.G.; Kockelmann, W.; Law, C.; Li, X.; Foglia, F.; Walsh, A.; O'Regan, *et al.*. The Dynamics of Methylammonium Ions in Hybrid Organic–Inorganic Perovskite Solar Cells. *Nat. Commun.,* **2015**, *6*, 7124:11.
(31) Bakulin, A.A.; Selig, O.; Bakker, H.J.; Rezus, Y.L.A.; Müller, C.; Glaser, T.S.; Lovrincic, R.; Sun, Z.; Chen, Z.; Walsh, A. *et al.* Real-Time Observation of Organic Cation Reorientation in Methylammonium Lead Iodide Perovskites. *J. Phys. Chem. Lett.* **2015**, *6*, 3663−3669.
(32) Mattoni, A.; Filippetti, A.; Saba, M.I.; Caddeo, C.; Delugas, P. Temperature Evolution of Methylammonium Trihalide Vibrations at the Atomic Scale. *J. Phys. Chem. Lett*. **2016**, *7*, 529−535.
(33) Keen, D.A.; Goodwin, A.L, The crystallography of correlated disorder. Nature, **2015**, *521*, 303-309.
(34) Egami, T.; Billinge, S.J.L. *Underneath the Bragg Peaks: Structural Analysis of Complex Materials*, Pergamon Press / Elsevier, **2003**, 1−424.
(35) Filippetti, A.; Delugas, P.; Saba, M.I.; Mattoni, A. Entropy-Suppressed Ferroelectricity in Hybrid Lead-Iodide Perovskites. *J. Phys. Chem. Lett*. **2015**, *6*, 4909−4915.
(36) Lahnsteiner, J.; Kresse, G.; Kumar, A.; Sharma, D.D.; Franchini, C.; Bokdam, M. Room Temperature Dynamic Correlation between Methylammonium Moelcuels in Lead-iodine Based Perovskite: An Ab-initio Molecular Dynamics Perspective. Preprint available online at arxiv.org/abs/1608.04991 (26 Oct 2016).
(37) Chen, Q.; Zhang, C.; Zhu, M.; Liu, S.; Siemens, M.E.; Gu, S.; Zhu, J.; Shen, J.; Wu, X.; Liao, C *et al.* Efficient Thermal Conductance in Organometallic Perovskite $CH_3NH_3PbI_3$ Films. *Appl. Phys. Lett.* **2016**, *108*, 081902:6.
(38) Panzer, F.; Bässler, S.; Hüttner, S.; Köhler, J.; Moos, R.; Thelakkat, M.; Hildner, R.; Köhler, A. Reversible Laser Induced Amplified Spontaneous Emission from Coexisting Tetragonal and Orthorhombic Phases in Hybrid Lead Halide Perovskites. *Adv. Optical Mater.,* **2016**, *4*, 917–928.
(39) Zacharias M.; Giustino M. One-Shot Calculation of Temperature-Dependent Optical Spectra and Phonon-Induced Band-Gap Renormalization. *Phys. Rev. B,* **2016**, *94,* 075125:19.
(40) www.isis.stfc.ac.uk/support-laboratories/materials-characterisation-lab/rigaku-miniflex-60015292.html (26 Oct 2016).
(41) www.isis.stfc.ac.uk/instruments/tosca/ins-database (26 Oct 2016).
(42) Clark, S.J.; Segall, M.D.; Pickard, C.J.; Hasnip, P.J.; Probert, M.J.; Refson, K.; Payne, M.C. First Principles Methods Using CASTEP. *Zeit. für Kryst.*, **2005**, *220*, 567−570.
(43) Perdew, J.P.; Burke, K.; Ernzerhof, M. Generalized Gradient Approximation Made Simple. *Phys. Rev. Lett.*, **1996**, *77*, 3865−3868.
(44) Tkatchenko, A.; Scheffler, M. Accurate Molecular Van Der Waals Interactions from Ground-State Electron Density and Free-Atom Reference Data. *Phys. Rev. Lett.*, **2009**, *102*, 073005−4.
(45) Łuczyńska, K.; Drużbicki, K.; Lyczko, K.; Dobrowolski, J.Cz. Experimental (X-ray, ^{13}C CP/MAS NMR, IR, RS, INS, THz) and Solid-State DFT Study on (1:1) Co-Crystal of Bromanilic Acid and 2,6-Dimethylpyrazine. *J. Phys. Chem. B*, **2015**, *119*, 6852–6872.
(46) Krzystyniak, M.; Drużbicki, K.; Fernandez-Alonso, F. Nuclear Dynamics in the Metastable Phase of the Solid Acid Caesium Hydrogen Sulfate. *Phys. Chem. Chem. Phys*, **2015**, *17*, 31287−31296.
(47) Refson, K.; Clark, S.J.; Tulip, P.R. Variational Density-Functional Perturbation Theory for Dielectrics and Lattice Dynamics. *Phys. Rev. B:* **2006**, *73*, 155114:12.
(48) Ramirez-Cuesta, A.J. aCLIMAX 4.0.1, The New Version of the Software for Analyzing and Interpreting INS Spectra. *Comput. Phys. Commun.*, **2004**, *157*, 226−238.
(49) Champion, D.; Tomkinson, J.; Kearley, G. a-CLIMAX: a New INS Analysis Tool. *Appl. Phys. A: Mater. Sci. Process.,* **2002**, *74*, S1302−S1304.
(50) Róg, T.; Murzyn, K.; Hinsen, K.; Kneller, G.R. nMoldyn: A Program Package for a Neutron Scattering Oriented Analysis of Molecular Dynamics Simulations. *J. Comput. Chem.*, **2003**, *24*, 657−667.